ADVANCED ENERGY MATERIALS

www.advenergymat.de

# Chemical Synthesis of 3D Graphene-Like Cages for Sodium-Ion Batteries Applications

*Xinxin Cao, Anqiang Pan,* Sainan Liu, Jiang Zhou, Site Li, Guozhong Cao, Jun Liu,* and Shuquan Liang**

**Sodium (Na) super ion conductor structured $Na_3V_2(PO_4)_3$ (NVP) is extensively explored as cathode material for sodium-ion batteries (SIBs) due to its large interstitial channels for $Na^+$ migration. The synthesis of 3D graphene-like structure coated on NVP nanoflakes arrays via a one-pot, solid-state reaction in molten hydrocarbon is reported. The NVP nanoflakes are uniformly coated by the in situ generated 3D graphene-like layers with the thickness of 3 nm. As a cathode material, graphene covered NVP nanoflakes exhibit excellent electrochemical performances, including close to theoretical reversible capacity (115.2 mA h $g^{-1}$ at 1 C), superior rate capability (75.9 mA h $g^{-1}$ at 200 C), and excellent cyclic stability (62.5% of capacity retention over 30000 cycles at 50 C). Furthermore, the 3D graphene-like cages after removing NVP also serve as a good anode material and deliver a specific capacity of 242.5 mA h $g^{-1}$ at 0.1 A $g^{-1}$. The full SIB using these two cathode and anode materials delivers a high specific capacity (109.2 mA h $g^{-1}$ at 0.1 A $g^{-1}$) and good cycling stability (77.1% capacity retention over 200 cycles at 0.1 A $g^{-1}$).**

Recently, sodium-ion batteries (SIBs) have attracted wide attention for large-scale energy storage systems due to the abundant supply of sodium.[1–5] SIBs are also a good alternation to lithium-ion batteries (LIBs) because both are based on cation intercalation electrode materials.[6–8] However, the larger $Na^+$ leads to sluggish ion diffusion and severe structural distortion of the host materials.[9–11] Consequently, large interstitial space and open crystallographic structure are needed to obtain good sodium storage properties.[12–14]

To date, a wide range of materials, such as metal oxides,[11,12,15,16] phosphates,[17–22] sulfates,[23–25] fluorophosphates,[26–28] and ferrocyanides,[29–31] have been investigated as sodium hosts. Among these, sodium (Na) super ion conductor (NASICON) structured $Na_3V_2(PO_4)_3$ (NVP) is a good candidate cathode material due to its excellent structural stability, good thermal stability, and high energy density.[18,32] In addition, the NASICON structure also has an open 3D framework and large interstitial channels for fast $Na^+$ ion diffusion. However, similar to other polyanion compounds (i.e., $Li_3V_2(PO_4)_3$ and $K_3V_2(PO_4)_3$),[33,34] NVP suffers from intrinsically inferior electronic conductivity (about $10^{-9}$ S $cm^{-1}$).

Two key strategies are applied to improve the conductivity of NVP. First, nanostructured NVP has been demonstrated to improve the sodium ion diffusion kinetics due to the reduced ion diffusion distance.[35–37] Zhou et al. reported template-assisted synthesis of nanostructured NVP 3D foams, which exhibit a capacity of 73 mA h $g^{-1}$ at a rate of 100 C.[35] An et al. prepared NVP/C nanoflakes with high rate capability and excellent cycling stability.[36] Making NVP and carbon composites can also improve the electronic conductivity and electrochemical performances. Saravanan et al. reported the preparation of porous NVP/C with good rate capability and long cycle life (30000 cycles at 40C).[38] Zhu et al. designed NVP embedded in a porous carbon matrix with high rate capability of 44 mA h $g^{-1}$ at 200C.[39] Klee et al. recently reported an oleic acid-based surfactant-assisted solid reaction method, which produced a uniform carbon coating on NVP nanoparticles and improved properties.[40] In addition, graphite-like carbon coating was applied by chemical vapor deposition or mechanical mixing.[21,22,41–43]

Herein, we report a detailed study of the formation of graphene-like cages structures on NVP nanoflake (NVP-NFs) arrays using the solid-state reaction approach in a molten surfactant-paraffin media.[44,45] As illustrated in **Figure 1**a, The NVP nanoflakes are uniformly capped with a graphene-like carbon layer, which are in situ generated in the calcination process. The graphene-like layers are connected each other to form a 3D conductive carbon network. The unique architecture provides a large contact area between electrode and electrolyte and fast electron diffusion pathway. As a cathode material for SIBs, the NVP-NFs encapsulated in the 3D graphene-like cages manifest close to theoretical capacity, excellent rate capability, and ultralong-life cycling performance. In addition, the NVP can

Dr. X. X. Cao, Prof. A. Q. Pan, Dr. S. N. Liu, Dr. J. Zhou, Dr. S. T. Li, Prof. S. Q. Liang
School of Material Science and Engineering
Central South University
Changsha 410083, P. R. China
E-mail: pananqiang@csu.edu.cn; lsq@csu.edu.cn
Prof. G. Z. Cao
Department of Materials Science & Engineering
University of Washington
Seattle, WA 98195, USA
Dr. J. Liu
Pacific Northwest National Laboratory
Richland, WA 99352, USA
E-mail: jun.liu@pnnl.gov

**DOI: 10.1002/aenm.201700797**

 

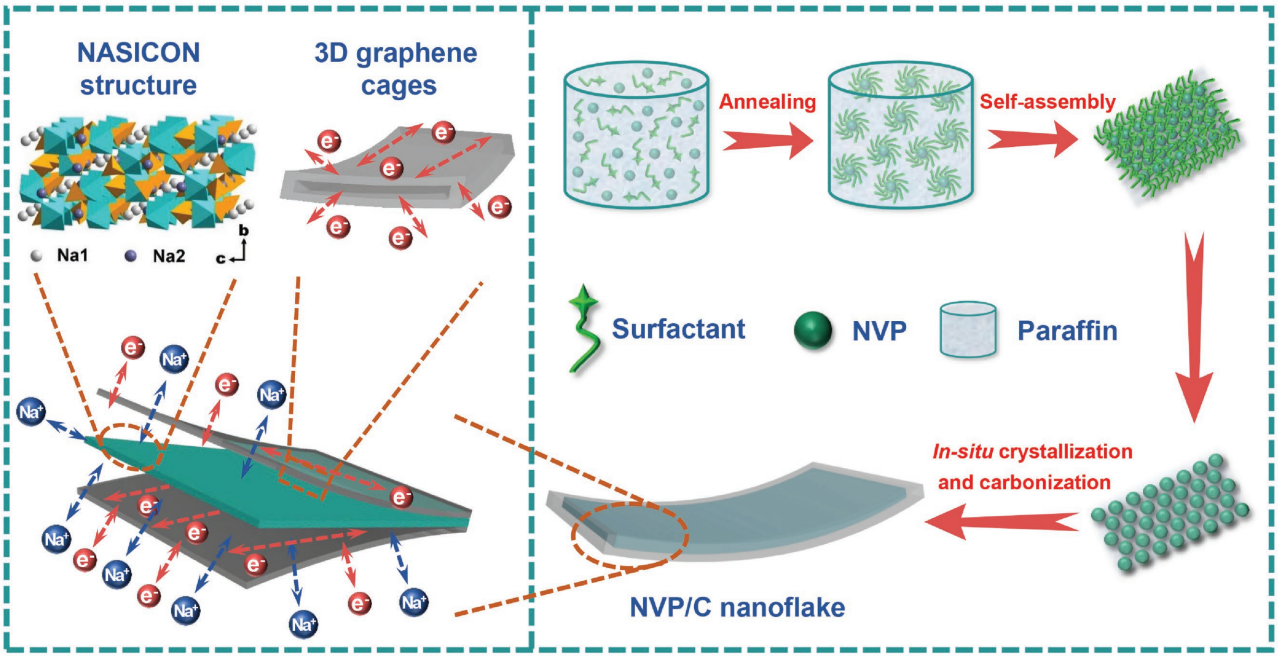


**Figure 1.** Schematic illustration of the fabrication of 3D graphene capped NVP-NFs. a) Schematic illustration of the 3D graphene coated NVP-NFs with pathways for both electrons and sodium ions. b) Schematic illustration for the fabrication process and the proposed formation mechanism.

be removed to leave a hollow 3D graphene-like material which can serve as a good anode material for sodium ion storage. The graphene encapsulated NVP-NFs cathode and 3D graphene-like anode can be assembled into full-cells to deliver a high specific capacity and good cycling stability.

Figure 1b schematically illustrates the formation process of graphene capped NVP-NFs. In this work, the 3D graphene coated NVP-NFs are synthesized via a facile solid-state method in molten hydrocarbon media where oleic acid acts as a surfactant, and paraffin serves as a nonpolar solvent. Oleic acid is a typical anionic surfactant with a high-polarity carboxyl group, an unsaturated bond, a long alkyl chain, and a nonpolar tail. Paraffin is a commonly used hydrophobic alkane solvent, which can provide a stable environment for moisture-sensitive precursors. First, the $NH_4H_2PO_4$, $VOC_2O_4 \cdot nH_2O$, $CH_3COONa$, and oleic acid were homogeneously distributed in the paraffin wax matrix to form a viscous precursor mixture in the high-energy ball-milling process. The carboxyl group in oleic acid was attached to the sodium–vanadium–phosphate complex with hydrophobic tail exposed to the paraffin media during the sintering process at low temperature (<300 °C).[44,46] According to the thermogravimetry (TG) and differential scanning calorimetry analysis results, most of the excess oleic acid and paraffin were removed from the mixture between 250 and 400 °C, leaving only a capping layer on the surface (Figure S1, Supporting Information). The NVP nanocrystals start to form at 400 °C, accompanied by the decomposition of sodium–vanadium–phosphate complex (Figures S1–S3, Supporting Information). Meanwhile, the presence of the long alkyl chain and unsaturated bond in oleic acid promotes the crystallization and growth of the NVP nanocrystals.[47,48] Finally, the NVP nanocrystals assemble into nanoflake morphology when the temperature is raised to 800 °C (Figures S1 and S2, Supporting Information).

**Figure 2**a shows the powder XRD pattern of the prepared NVP-NFs. All the diffraction peaks can be readily indexed to the rhombohedral NASICON structure (space group $R\bar{3}c$, ICSD#98-024-8140), with no extraphases or crystalline carbon diffraction peaks. Figure 2b shows the Raman scattering spectrum of NVP-NFs. The characteristic bands in the range of 200–1100 $cm^{-1}$ are the Raman fingerprint characteristics of NVP.[18,32] The two broad and intense bands located around at 1350 and 1590 $cm^{-1}$ are attributed to the D-band (disorder-induced phonon mode) and G-band ($E_{2g}$ vibrations of graphite), respectively. The ratio of the peak intensities of D to G band ($I_D/I_G$) is around 0.99, indicating a relatively high degree of graphitization. The high graphitization degree is beneficial for achieving good electronic conductivity.[22,36] According to the TG measurement result, the weight percentage of carbon in the NVP-NFs composite is about 8.4% (Figure S4, Supporting Information). The NVP-NFs were further characterized by Fourier transform infrared spectroscopy (FT-IR) in Figure 2c. The bands at 580 and 1048 $cm^{-1}$ are assigned to the P—O bonds in $PO_4$ tetrahedra while the band at 631 $cm^{-1}$ is assigned to the vibration from $V^{3+}$—$O^{2-}$ bonds in isolated $VO_6$ octahedra.[35] Moreover, the infrared bands in the range of 1150–1250 $cm^{-1}$ can be attributed to the stretching vibration of $PO_4$ units.[35] X-ray photoelectron spectroscopy (XPS) measurements were also conducted to probe the chemical components and oxidation states of the as-prepared NVP-NFs (Figure 2d). The five elemental signals, namely C 1s, O 1s, Na 1s, P 2s, P 2p, and V 2p peaks, are observed in the XPS spectrum of NVP-NFs. Figure 2e shows the binding energy for V $2p_{3/2}$ at ≈515.5 eV, which is in good agreement with $V^{3+}$ in NVP.[49–51] The results also confirm the good crystallinity of the obtained NVP phase.

The graphene encapsulated NVP-NFs were characterized by nitrogen adsorption–desorption technique as shown in Figure 2f.

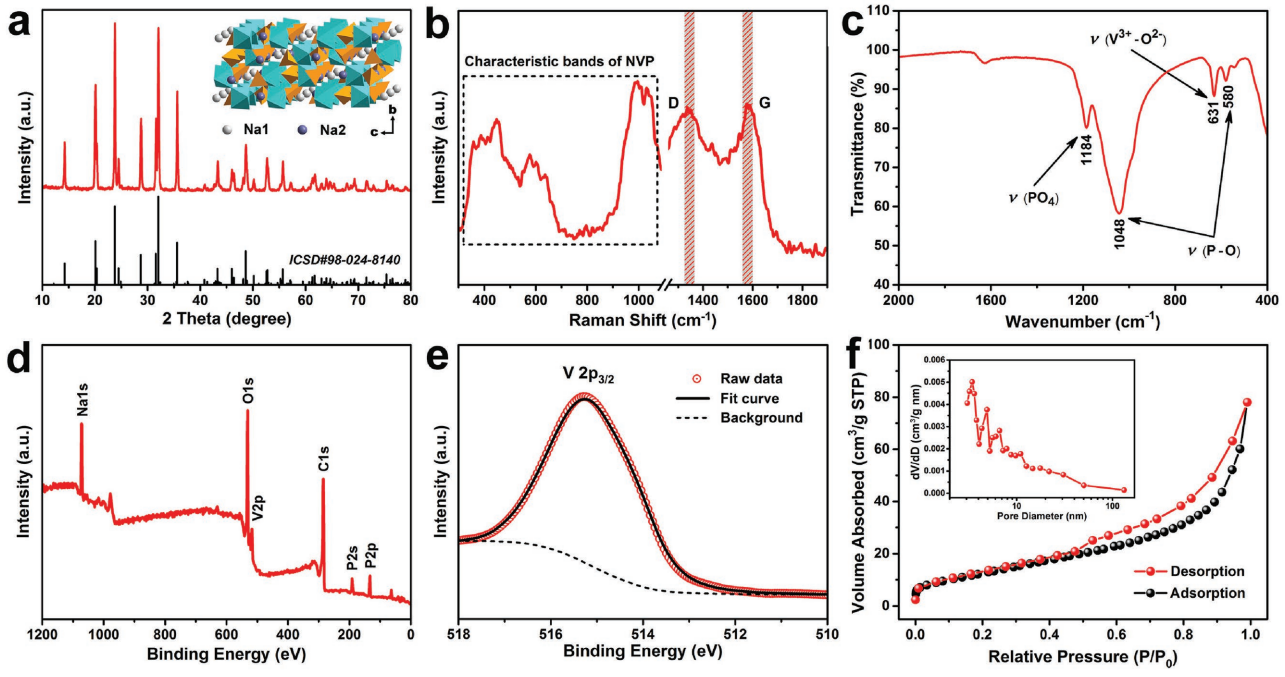


**Figure 2.** The chemical and physical characterizations of the as-prepared NVP-NFs. a) X-ray diffraction pattern. b) Raman scattering spectrum. c) FTIR spectra. d,e) XPS spectrum. f) Nitrogen adsorption–desorption isotherm and corresponding pore size distribution curve (the inset).

The isotherm can be described as type II with a H3 hysteresis loop, which can be linked to slit-shaped pores in the sample. According to the Brunauer–Emmet–Teller (BET) method, the surface area of NVP-NFs is 33.54 $m^2$ $g^{-1}$. The Barret–Joyner–Halenda pore size distribution curve (the inset of Figure 2f) indicates the majority of the pores in NVP-NFs are less than 20 nm.

The morphology and microstructure of the NVP-NFs composite were investigated by field emission scanning electron microscopy (FESEM) and transmission electron microscopy (TEM). As shown in SEM images in **Figure 3**a,b, the nanoflake arrays are loosely interconnected with obvious open spaces between them. The uniform nanoflakes have smooth surface with an approximately thickness of 20–30 nm and an in-plane extension of about 200–300 nm. The TEM images (Figure 3c,d) further reveal that the array-like architecture is actually made of numerous ultrathin nanoflakes, and the NVP-NFs are capped with an in situ generated 3D graphene-like carbon structure. A carbon layer with rough seven to eight graphene nanosheets can also be observed on the surface of the NVP nanoflake (the inset of Figure 3d). This unique structure can provide fast electron transportation and shorten the sodium ion diffusion distances. The high-resolution TEM (HRTEM) image (Figure 3e) shows clear lattice fringes with *d*-spacings of 4.1 and 6.8 Å, which correspond to the interplanar distance of the $(\bar{2}10)$ and $(01\bar{1})$ planes of rhombohedral NVP crystal, respectively. The selected area electron diffraction (SAED) pattern (the inset of Figure 3e) further reveals the single-crystalline nature of NVP-NFs, and can be indexed to the [122] zone axis. In addition, the high angle annular dark field scanning TEM (HAADF-STEM) images demonstrate the uniform distribution of C, P, and V in the nanoflakes, suggesting the high quality of the composite (Figure 3f).

The 3D morphology and microstructure of graphene carbon scaffold were further investigated by acid leaching of NVP-NFs. The energy dispersive X-ray (EDX) spectrum (the inset of Figure 3g) demonstrates that the NVP crystals are totally removed by hydrochloric acid and only a carbon matrix is retained. After leaching, the uniform nanoflake structure is largely maintained with no discernible structural collapse in the matrix (Figure 3g). In particularly, an interconnected 3D graphene carbon scaffold can be clearly obtained (Figure 3h). The HRTEM image (Figure 3i) clearly reveals the lattice fringes of 0.34 nm, corresponding well with the *d*-spacing of the interplanar distance of the graphite. Furthermore, the graphene carbon scaffold was investigated by nitrogen adsorption–desorption analysis (Figure S5, Supporting Information). The 3D graphene scaffold has a BET surface area of 279.62 $m^2$ $g^{-1}$ and the majority of pores less than 20 nm. Moreover, the pore volume can be as large as 0.868 $cm^3$ $g^{-1}$. This robust architecture with 3D conductive graphene-like carbon layers are rarely reported.

For comparison, similar experiments without adding paraffin wax or oleic acid were carried out and only NVP nanoparticles (NVP-NPs) and NVP bulk particles (NVP-BPs) were obtained, respectively (Figures S6 and S7, Supporting Information). In the absence of paraffin wax matrix, only nanoparticle morphology is obtained (Figure S6, Supporting Information). The result demonstrates that the existence of paraffin wax can improve the homogeneity dispersion of oleic acid in the mixture, which facilitates the NVP crystallization and growth during the high-temperature synthesis process. However, non-uniform bulk particles with the diameter about 0.5–2 µm were produced without adding oleic acid (Figure S7, Supporting Information). The result indicates that the growth of NVP was

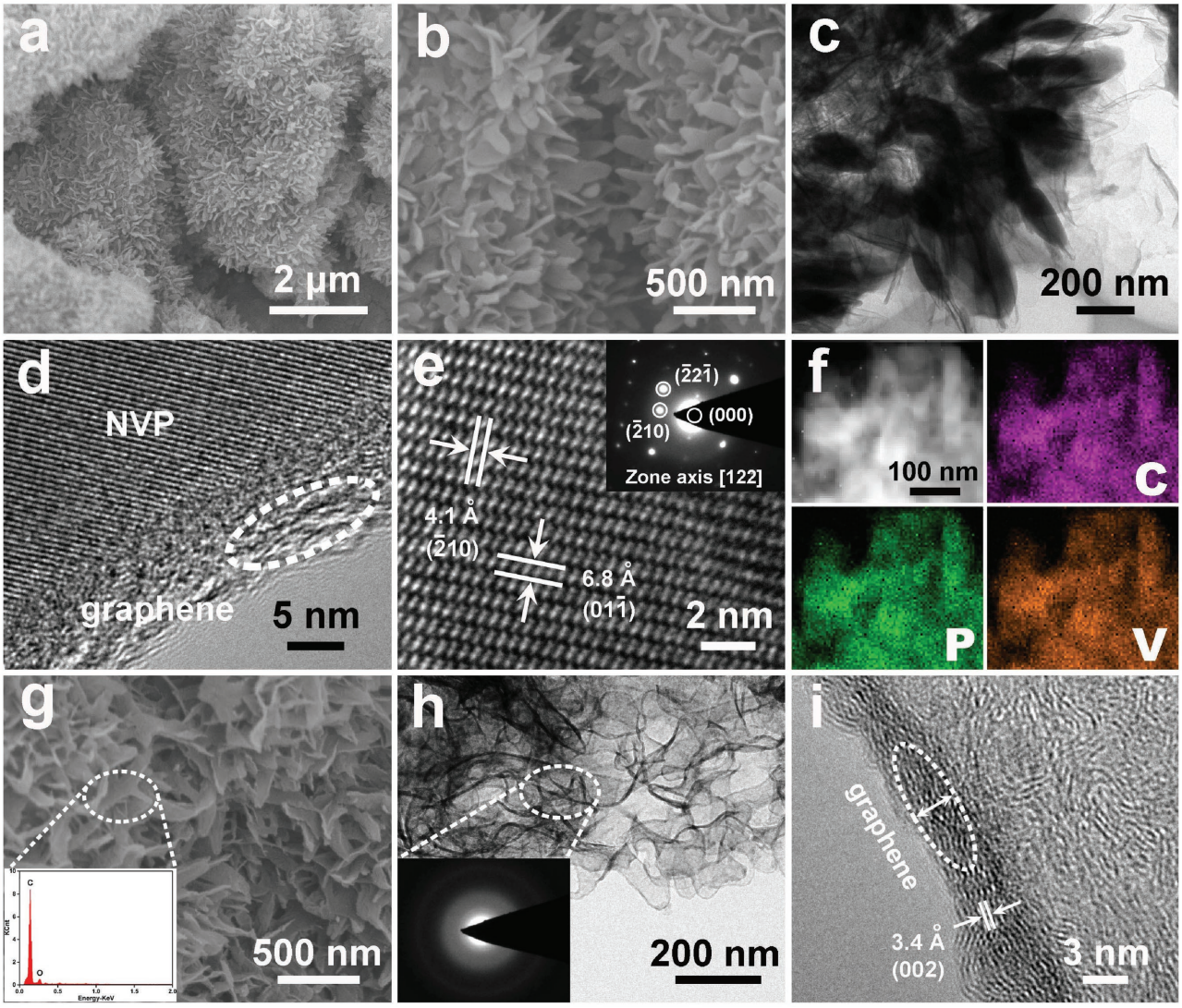


**Figure 3.** The morphological and microstructural characterizations of the as-prepared NVP-NFs and the pure 3D graphene scaffold after the corrosion of NVP nanoflakes. a,b) FESEM images at low and high magnifications. c) TEM image. d,e) HRTEM images and the corresponding SAED pattern (the inset of panel (e)). f) STEM-HAADF images. g) FESEM image, h) TEM image, and i) HRTEM image of the 3D graphene carbon scaffold; the insets of panels (g) and (h) are the EDX spectrum and SAED pattern of the selected regions, respectively.

limited by the surface capping of oleic acid on the surface of the precursor. The chemical and physical characterizations of the two samples are shown in Figures S8–S11 (Supporting Information). Pure NVP with good crystallinity (Figures S6d and S7d, Supporting Information) was obtained and no carbon diffraction peaks were detected (Figures S8 and S9, Supporting Information). Moreover, the NVP-NPs and NVP-BPs samples have a BET surface area of 25.95 and 5.23 $m^2\ g^{-1}$ (Figure S8f, Supporting Information), respectively. Furthermore, the TG analysis result demonstrates that the carbon content in the two samples are about 6.7 and 1.5 wt%, respectively (Figure S11, Supporting Information). The result also confirms that oleic acid is the main carbon source during the synthesis process.

The NVP-NFs were first assembled into half-cells to evaluate their electrochemical performances as cathode materials for sodium-ion batteries and the results are shown in **Figure 4**. Figure 4a presents the initial five successive cyclic voltammetry (CV) profiles at a scan rate of 0.1 mV $s^{-1}$, which are almost identical with no apparent peak intensity or position changes. The results demonstrate their good reversibility during the repeated cycling process.[52] The cathodic peak at 3.32 V and anodic peak at 3.51 V corresponds to the $V^{3+}/V^{4+}$ redox couple with two $Na^+$ extraction/insertion in the NVP lattice (i.e., $Na_3V_2(PO_4)_3 - 2Na^+ - 2e^- \leftrightarrow NaV_2(PO_4)_3$).[38] According to this reaction, two ions are oxidized from $V^{3+}$ to $V^{4+}$ per $Na_3V_2(PO_4)_3$ molecule corresponding to a theoretical capacity of 117.6 mA h $g^{-1}$. The cathodic performance of the as-prepared NVP materials was evaluated by using the galvanostatic charge–discharge technique. Figure 4b shows the selected charge–discharge profiles of the first, second, and fifth cycles for the NVP-NFs at the rate of 1C. Here 1C refers to 117.6 mA $g^{-1}$. The charge and discharge plateaus are located at 3.48 and 3.33 V, respectively,

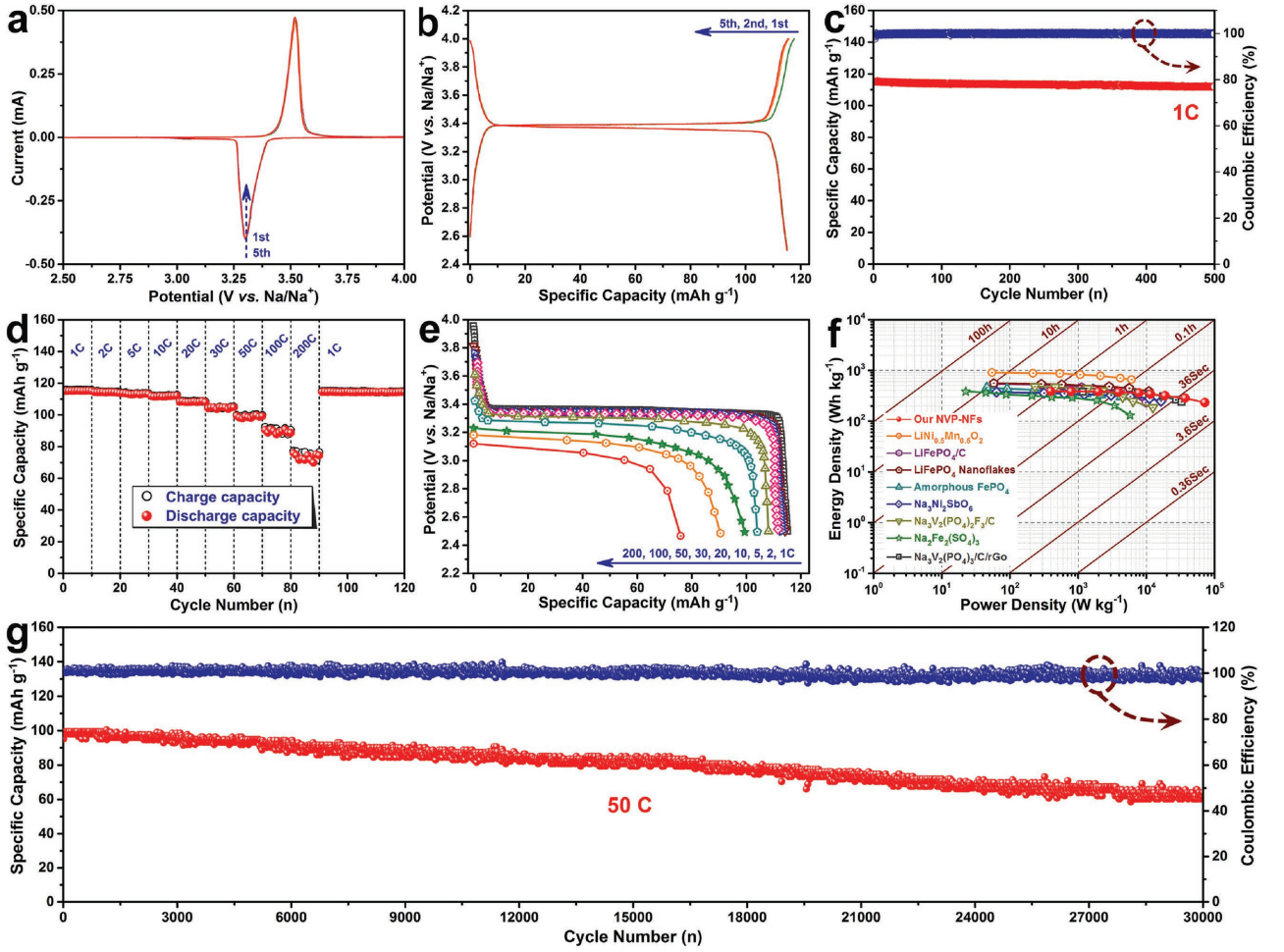


**Figure 4.** The electrochemical characterization of the as-prepared NVP-NFs as a half-cell cathode in the potential range of 2.5–4.0 V versus $Na/Na^+$. a) Initial five cyclic voltammograms at a scan rate of 0.1 mV $s^{-1}$. b) The first, second, and fifth charge–discharge profiles at a current density of 1 C (1 C = 117.6 mA $g^{-1}$). c) Cycling performance at the current density of 1 C. d) Rate capability and the corresponding e) galvanostatic discharge profiles at various current densities from 1 C to 200 C. f) Ragone plots of our NVP-NFs cathode, compared with some advanced LIBs and SIBs cathode materials ($LiNi_{0.5}Mn_{0.5}O_2$||Li,[54] $LiFePO_4$/C||Li,[56] $LiFePO_4$ nanoflakes||Li,[57] amorphous $FePO_4$||Li,[58] $Na_3Ni_2SbO_6$||Na,[59] $Na_3V_2(PO_4)_2F_3$||Na,[60] $Na_2Fe_2(SO_4)_3$||Na,[23] and $Na_3V_2(PO_4)_2$/C/rGO||Na).[18] g) Ultralong-life cycling performance and Coulombic efficiency for 30000 cycles at 50 C.

which are in good agreeement with the CV results. The 3D graphene capped NVP-NFs exhibit the initial charge and discharge capacities of 117.2 and 115.1 mA h $g^{-1}$, respectively, corresponding to a high Coulombic efficiency of 98.2%. Obvious discharge/charge plateaus are observed from the two phase transition between $Na_3V_2(PO_4)_3$ and $NaV_2(PO_4)_3$. Interestingly, only a small initial charge capacity loss was detected, which can be attributed to the electrolyte decomposition and other undesirable side reactions.[12,32,53] However, the charge and discharge profiles in the subsequent cycles are almost identical, indicating excellent reversibility of the NVP-NFs electrodes. Figure 4c shows the cycling behaviors of the graphene coated NVP-NFs cathodes at 1 C rate. The NVP-NFs electrode delivers an initial discharge capacity of 115.2 mA h $g^{-1}$, very close to the theoretical capacity. After 500 cycles, a discharge capacity of 112.0 mA h $g^{-1}$ can be retained, corresponding to 97.2% of its initial capacity. Figure S12 (Supporting Information) shows the cycling performance of the NVP-NFs cathode with different areal mass loading increasing from 1.24 to 5.36 mg $cm^{-2}$ at 1 C. Even at a high active material mass loading of 5.36 mg $cm^{-2}$, a discharge capacity of 90 mA h $g^{-1}$ (77.0% of the theoretical capacity) is still delivered, further indicating the high availability of the active material.

The rate performance of NVP-NFs is also investigated and the result is shown in Figure 4d. The NVP-NFs exhibit the discharge capacities of 115.2 to 114.2, 113.1, 111.6, 108.1, 104.0, 99.4, and 90.5 mA h $g^{-1}$ at the rates of 1 C, 2 C, 5 C, 10 C, 20 C, 50 C and 100 C, respectively. Even at an ultrahigh rate of 200C, a reversible capacity of 75.9 mA h $g^{-1}$ is available. This excellent rate performance is comparable to that of a supercapacitor.[54,55] Notably, even after long cycles with different rates, when the current rate is reverted to 1 C, a high discharge capacity of 114.5 mA h $g^{-1}$ (99.4% of the initial capacity) is recovered. The results demonstrate the excellent rate capability of the NVP-NFs electrode for $Na^+$ ion storage. For comparison, the rate capabilities of NVP-NPs and NVP-BPs were also evaluated (Figures S13 and S14, Supporting Information). Compared with those of NVP-NPs and NVP-BPs (Figure 4d; Figures S13a, S14a, and S15,

Supporting Information), the 3D graphene capped NVP-NFs exhibit remarkable enhanced rate performance at different rates (especially at high rates). Figure 4e shows the discharge voltage plateaus at different rates. Even at the rates larger than 20 C, the plateaus still can be clearly presented. Moreover, the small plateau voltage difference at different rates suggests the low polarization of the NVP-NFs electrode. The polarization is much smaller than those for the NVP-NPs and NVP-BPs electrodes (Figures S13b, S14b, and Table S1, Supporting Information). In general, the polarization of the electrode materials is largely caused by the electron transportation resistances. The graphene coating on the NVP-NFs significantly improves the electron conductivity of the electrode materials, thus lowering polarization is detected.

Figure 4f shows Ragone plot of the NVP-NFs, and some advanced LIBs and SIBs cathode materials (normalized to the weight of cathode materials). The NVP-NFs cathode can achieve a high energy density of 387.3 W h $kg^{-1}$ at a low power density of 397.1 W $kg^{-1}$. Even at a maximum power density of 72 kW $kg^{-1}$ (charge and discharge time of 18 s), the device still possesses an energy density of 231.9 W h $kg^{-1}$, indicating that the high energy and power densities would be simultaneously obtained. The result even compares well with the current state-of-the-art cathodes such as $LiNi_{0.5}Mn_{0.5}O_2$,[54] $LiFePO_4$/C,[56] $LiFePO_4$ nanoflakes,[57] amorphous $FePO_4$,[58] $Na_3Ni_2SbO_6$,[59] $Na_3V_2(PO_4)_2F_3$,[60] $Na_2Fe_2(SO_4)_3$,[23] and $Na_3V_2(PO_4)_2$/C/rGO.[18] The good electrochemical performance is highly desirable for high-power SIBs applications such as hybrid electric vehicles, electric vehicles, and large-scale energy storage systems.

Moreover, the long-term cycling stability of the NVP-NFs has been studied. The NVP-NFs can retain more than 92.3% of the initial cyclic capacity at 5 C after 3000 cycles, and can retain 83.1% of its original capacity after 10000 cycles at 20 C (Figure S16 and Table S2, Supporting Information). Moreover, the NVP-NFs deliver an initial specific discharge capacity of 99.4 mA h $g^{-1}$ at the current rate of 50 C and retain a capacity of 62.1 mA h $g^{-1}$ after 30000 cycles, with the capacity retention of 62.5% and average capacity fading rate of 0.0013% per cycle (Figure 4g). The Coulombic efficiencies under various rates are around 100%, indicating the superior phase reversibility of the NVP-NFs electrode material during repeated extraction/insertion of $Na^+$ ion at high current rates. However, the long-term cycling performances of the other two cathodes are much inferior. The NVP-NPs electrode only retain a reversible capacity of 52 mA h $g^{-1}$ after 20000 cycles at 50 C (Figure S13c, Supporting Information), and the NVP-BPs deliver almost no capacity after 5000 cycles at 50 C (Figure S14c, Supporting Information). The specific capacity, rate capability, and cyclic stability for NVP-NFs cathode are better than the state-of-the-art reported NVP cathodes (Table S3, Supporting Information).

To further demonstrate the versatility of the prepared product, the pure 3D graphene-like framework was tested as anode materials to investigate sodium ion storage capability. **Figure 5**a shows the typical charge–discharge profiles of the pure 3D graphene-like cages using sodium metal as counter electrode at a current density of 0.1 A $g^{-1}$. The second discharge and charge capacities are 276 and 236 mA h $g^{-1}$, respectively, and the large irreversible capacity can be assigned to the formation of an SEI layer on the anode material, in particular for those with high surface area.[61,62] However, the Coulombic efficiency increases continuously for the later cycles. When cycled at a current density of 0.1 A $g^{-1}$, the 3D graphene electrode exhibits an initial charge capacity of 242.5 mA h $g^{-1}$ and maintains a capacity of 203.2 mA h $g^{-1}$ after 500 cycles (Figure 5b).

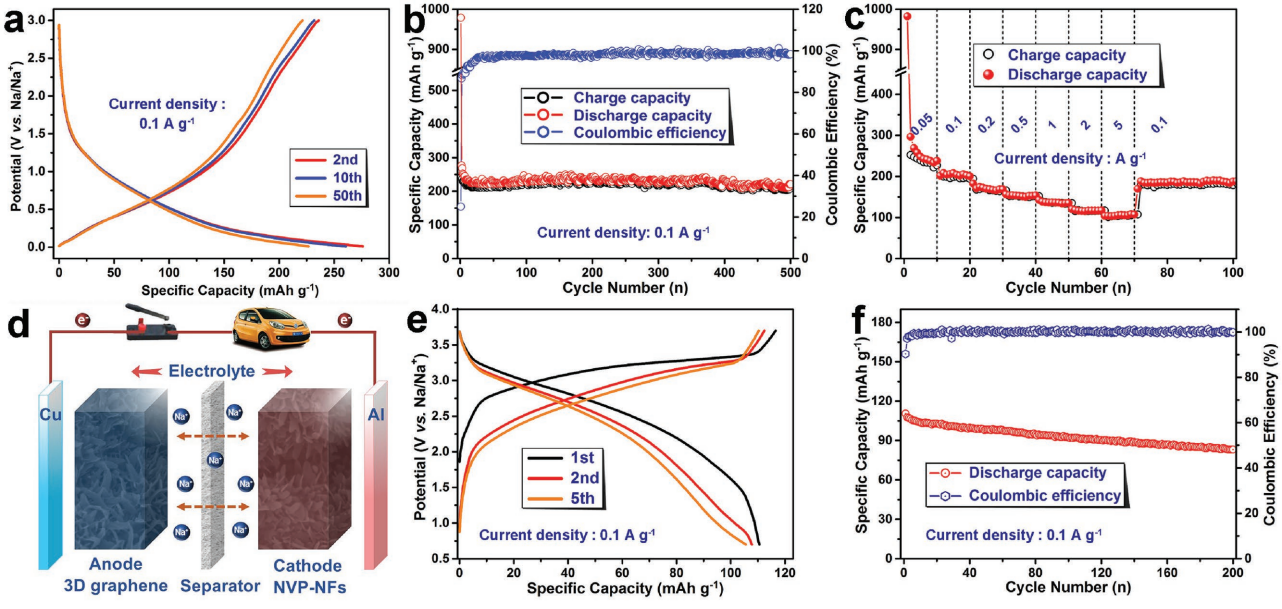


**Figure 5.** Electrochemical performance of the pure 3D graphene electrodes and the sodium-ion full-cells. a) Galvanostatic charge–discharge profiles, and b) cycling performance of the pure 3D graphene scaffold as a half-cell anode in the potential range of 0.01–3.0 V (vs $Na/Na^+$) at a current density of 0.1 A $g^{-1}$. c) Rate capability of the 3D graphene electrodes in half-cell. d) Schematic of sodium-ion full-cell with NVP-NFs cathode and 3D graphene anode. e) Galvanostatic charge–discharge profiles of the sodium-ion full-cell in the potential range of 0.7–3.7 V at a current density of 0.1 A $g^{-1}$. f) Cycling performance of the full-cell at 0.1 A $g^{-1}$.

As shown in Figure 5c, the 3D graphene-like electrode also delivers a reversible capacity of 252.2, 207.7, 182.6, 156.5, 142.8, 120.4, and 103.8 mA h $g^{-1}$ at current densities of 0.05, 0.1, 0.2, 0.5, 1, 2, and 5 A $g^{-1}$, respectively, indicating excellent high rate capability. When the current density is reset to 0.1 A $g^{-1}$, a specific capacity of 188.3 mA h $g^{-1}$ can be restored. The electrochemical performances of 3D graphene-like cages are comparable to the state-of-the-art reported carbon-based anode materials for sodium-ion batteries.[61–64]

Based on the above results, a sodium-ion full-cell was constructed using NVP-NFs cathode and 3D graphene-like anode. Figure 5d illustrates the particular configuration of the full-cell and the potential applications. Figure 5e shows the selected charge–discharge profiles of the sodium-ion full-cell at a current density of 0.1 A $g^{-1}$. The full-cell displays a slope profile with an average operating potential of 2.7 V. It is observed that the initial charge and discharge capacities are 115.8 and 109.2 mA h $g^{-1}$, respectively, corresponding to an initial Coulombic efficiency of 94.3%. As shown in Figure 5f, the sodium-ion full-cell delivers an initial specific discharge capacity of 109.2 mA h $g^{-1}$ at 0.1 A $g^{-1}$ based on the weight of NVP-NFs cathode. After 200 cycles, it still can retain 84.2 mA h $g^{-1}$, 77.1% of its original capacity, indicating the good reversibility of the sodium-ion full-cell. On the basis of a comprehensive literature study (Table S4, Supporting Information), this sodium-ion full-cell combines both the advantages of high median voltage and high reversible capacity among all reported sodium-ion full-cell systems, to the best of our knowledge.

To better understand the electrochemical performance of the 3D graphene decorated NVP-NFs electrode, electrochemical impedance spectra (EIS), ex situ X-ray diffraction measurement (XRD), and TEM characterizations were performed. **Figure 6**a shows the CV curves of the NVP-NFs at various scan rates, which indicates that the current densities of the redox peaks increase with the larger scan rates. Figure 6b shows the correlation between the peak current density ($I_p$) and the square roots of the scanning rate ($v^{1/2}$), which fits a linear relationship nicely. The result demonstrates that the two-phase transition in NVP-NFs is diffusion controlled. The apparent diffusion coefficients of $Na^+$ are calculated based on the Randles–Sevcik equation (Note S1, Supporting Information), and $Na^+$ diffusion coefficient for the NVP-NFs composite is up to the order of magnitude of $10^{-10}$ $cm^2$ $s^{-1}$ for the $Na^+$ extraction/insertion processes.

The electrochemical impedance is also carried out to evaluate the charge transfer resistance and sodium ion diffusion coefficient for the electrodes. The Nyquist plots (Figure 6c) indicate that the charge transfer resistance ($R_{ct}$) of the NVP-NFs is only 68.08 Ω before cycling, much lower than that of the NVP-NPs (183.1 Ω) and NVP-BPs (333.8 Ω) (Figure S17 and Table S5, Supporting Information). Even after 500 cycles, only a small impedance increase is detected, suggesting fast electronic mobility of the NVP-NFs electrode (Figure 6c; Table S6, Supporting Information). The $Na^+$ diffusion coefficients of NVP-NFs electrode after different cycles, as well as NVP-NPs and NVP-BPs electrodes before cycling, are also calculated based on the Note S2 (Supporting Information) and linear relationship between $Z'$ versus $\omega^{-1/2}$ at low-frequency region (Figures S17b and S18, Supporting Information). The $Na^+$ ion diffusion coefficient of the NVP-NFs fresh electrode is calculated to be $2.53 \times 10^{-10}$ $cm^2$ $s^{-1}$, an order higher than the NVP-NPs

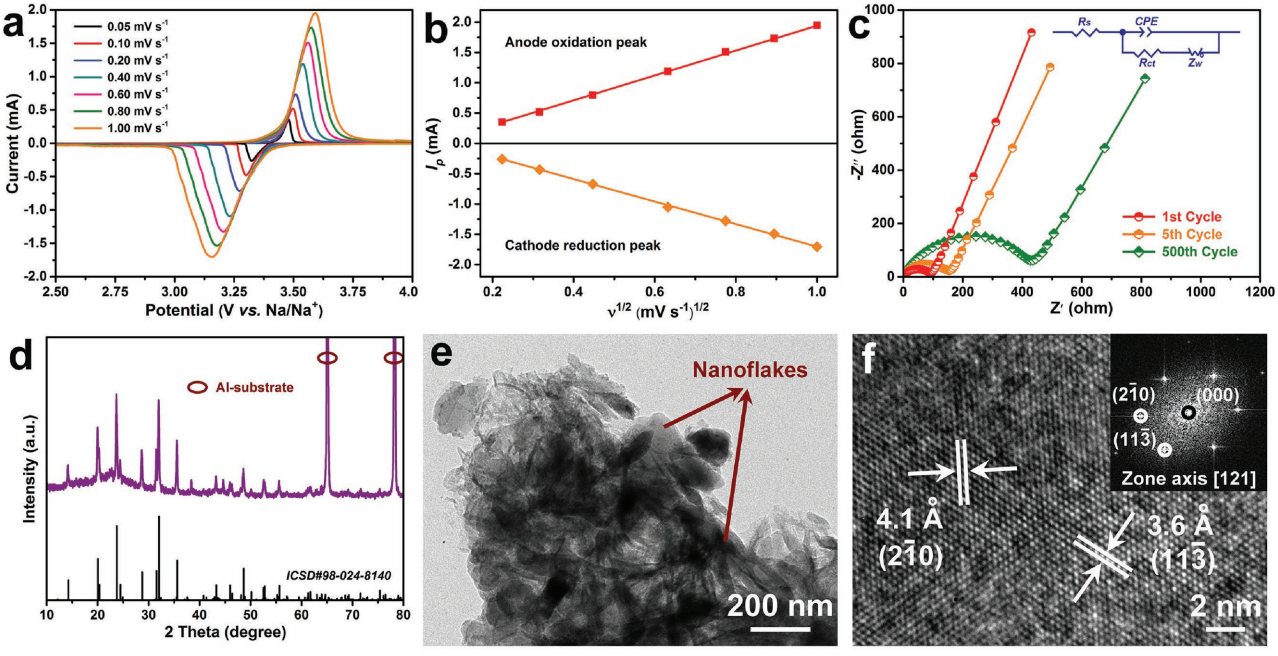


**Figure 6.** Kinetics analysis and ex situ characterization. a) Cyclic voltammograms of the as-prepared NVP-NFs cathode at various scan rates, and b) the corresponding linear fitting of the peak current ($I_p$) versus square root of scan rate ($v^{1/2}$). c) Nyquist plots of the NVP-NFs cathode after different cycles at 1 C and the corresponding fitted equivalent circuit model (the inset). ($R_s$: Ohmic resistance of solution and electrodes, $R_{ct}$: charge transfer resistance, CPE: double layer capacitance, $Z_w$: Warburg impedance.). Ex situ d) XRD, e) TEM, and f) HRTEM studies of the as-prepared NVP-NFs electrode after 10000 cycles at 20 C; the inset of panel (f) is the Fourier transform (FFT) image of the corresponding area.

($2.58 \times 10^{-11}$ cm$^2$ s$^{-1}$), and NVP-BPs ($4.10 \times 10^{-11}$ cm$^2$ s$^{-1}$) (Table S5, Supporting Information). Moreover, even after 500 cycles, the NVP-NFs electrode still exhibits rapid ion diffusion rate (Table S6, Supporting Information). In addition, the activation energies of the as-prepared NVP-NFs, NVP-NPs, and NVP-BPs electrodes are calculated based on the temperature dependent EIS and the Arrhenius plots of log $i_0$ as a function of $1/T$ (Note S3 and Figure S19, Supporting Information). The activation energies of NVP nanoflakes, nanoparticles, and bulk-particles electrodes at 3.3 V are calculated to be 21.1, 22.2, and 24.8 kJ mol$^{-1}$, respectively (Table S7, Supporting Information). The enhanced kinetics indicates that the 3D graphene carbon decorated NVP nanoflakes cathode greatly improves the ionic transport kinetics and electronic conductivity, and thus give the above-mentioned high-rate capability and excellent cycling stability. The ex situ XRD pattern of NVP-NFs electrode after 10000 cycles (Figure 6d) shows that, all the diffraction peaks can be well indexed to the rhombohedral NVP phase, implying the excellent structural integrity. The structural stability of the NVP-NFs was further studied by TEM (Figure 6e). The array-like architecture constructed by nanoflakes is well maintained even after 10000 cycles at 50C and no aggregation or pulverization are observed. In addition, the lattice fringes can be clearly observed, further demonstrating the highly ordered single-crystal structure of NVP even after 10000 fast cycles (Figure 6f). In this work, the well-crystallized array-like architecture is retained. The good structural integrity of the NVP electrode can be attributed to the intimately covered graphene on the surface of the NVP-NFs, which has excellent mechanical stability.

On the basis of the above results, the excellent electrochemical performance of NVP-NFs, including high reversible capacity, high rate capability, and excellent cyclic stability can be ascribed to the unique architecture. First, the unique ultrathin nanoflake arrays with large surface area can offer effective electrode–electrolyte contact area, easy electrolyte pathway, and shortened ion diffusion distance. Second, the robust 3D graphene carbon scaffold can improve the electron conductivity of the electrode. Third, the uniform nanoflakes conformally capped with graphene-like layers can keep the structural integrity of the electrode materials.

In summary, we have developed a facile molten hydrocarbon-assisted, solid-state reaction strategy to synthesize novel 3D graphene decorated NVP nanoflakes. When used as cathode for SIBs, the NVP-NFs exhibit a high reversible capacity of 115.2 mA h g$^{-1}$ at 1 C, which is very close to the theoretical capacity. Even at 200 C, the electrode can deliver a specific discharge capacity of 75.9 mA h g$^{-1}$. After the long-term 30000 cycles at the rates of 50 C, the electrode can still retain 62.5% its initial specific capacity. In addition, an advanced sodium-ion full-cell based on NVP-NFs cathode and 3D graphene anode delivers a high specific capacity of 109.2 mA h g$^{-1}$ at 0.1 A g$^{-1}$, as well as a high capacity retention of 77.1% over 200 cycles at 0.1 A g$^{-1}$. This remarkable electrochemical performance is attributed to the unique architecture and the favorable crystal structure, which provide the bicontinuous electron/ion transport pathways, large electrode–electrolyte contact area for rapid $Na^+$ diffusion and electron transport. Meanwhile, the robust structure can rapidly accommodate the volume variations during repeated $Na^+$ ion extraction/insertion. We believe that this work is an important milestone in the development of large-scale energy storage systems technologies.

## Experimental Section

*Materials Preparation*: All reagents used in this experiment were of analytically pure grade and were used directly without any further purification. First, $V_2O_5$ and $H_2C_2O_4{\cdot}2H_2O$, in a stoichiometric ratio of 1:3, were dissolved in distilled water under vigorous stirring at 75 °C until a dark blue solution was formed, which indicates the formation of $VO^{2+}$. After evaporating the water for several hours with continuously stirring, the $VOC_2O_4{\cdot}nH_2O$ was obtained for further use. The NVP-NFs was prepared by a one-pot, solid-state reaction in molten surfactant-paraffin media. In brief, $NH_4H_2PO_4$ was milled initially with oleic acid for 1 h using a QM-3B high-energy milling machine in a stainless steel vial with stainless steel balls. Subsequently, the paraffin wax was added and milled for another 1 h. Then, $VOC_2O_4{\cdot}nH_2O$ was added, and the mixture was milled for 0.5 h. Finally, $CH_3COONa$ was added and further milled for 0.5 h. The overall molar ratio of Na:V:P:oleic acid in the milling mixture is 3:2:3:3, in which the weight of paraffin wax doubles that of the oleic acid. The viscous precursor mixture was dried in an oven at 105 °C for 0.5 h, and subjected to heat treatment in tubular furnace at 800 °C for 8 h under an ultrahigh purity Ar-$H_2$ (95:5) atmosphere with a heating rate of 2 °C min$^{-1}$ to obtain the final NVP-NFs. As a controlled experiment, the NVP-NPs were prepared through a similar procedure mentioned above except for without adding paraffin wax and the NVP-BPs were obtained without adding oleic acid.

*Materials Characterization*: The crystal structure and phase composition of the obtained samples were characterized using X-ray diffraction measurement (Rigaku D/Max-2500 with nonmonochromated Cu K$\alpha$ radiation, $\lambda$ = 1.5418 Å). The carbon contents of the samples were determined by a thermalgravimetric analyzer (Netzsch STA449 C) and the property of carbon layer was analyzed by Raman spectrometer (LabRAM HR800). X-ray photoelectron spectroscopy (VG Escalab-250xi) measurements were also conducted to probe the electronic states of elements in the surface. Samples were further characterized using a FT-IR (AVTATAR, 370) based on the KBr wafer technique in the frequency range of 500–2500 cm$^{-1}$. The Brunauer–Emmett–Teller surface area was analyzed by the nitrogen adsorption–desorption isotherms, which was obtained from a NOVA 2200e surface area and pore size analyzer (Quantachrome Instruments) at 77 K. The microstructure and morphologies of the prepared samples were observed by FESEM (FEI Nova NanoSEM 230) at 10 kV. Transmission electron microscopy, HRTEM, and HAADF-STEM images were recorded with a FEI Tecnai G2 F20 electron microscope working at an acceleration voltage of 200 kV.

*Electrode Fabrication and Electrochemical Measurement*: The electrochemical measurements were carried out using two-electrode coin cells (CR2016). The cathodes were prepared by dispersing the as-prepared active materials (75 wt%), conductive Super P (15 wt%), and polyvinylidene fluoride (PVDF) (10 wt%) in *N*-methyl-2-pyrrolidone (NMP) solution to form a slurry. The homogeneous slurry was casted onto an aluminum foil, which served as current collector in the cathode, and then was dried in a vacuum oven at 100 °C overnight prior to cells assembly. The anodes were prepared by mixing active material (80 wt%), super P (10 wt%), and PVDF (10 wt%) dissolved in NMP, and then coated onto a copper foil and dried at 100 °C overnight before testing. For sodium-ion half-cell fabrication, the metallic sodium foil as the counter-electrode, the glass fiber membrane of 0.5 mm in thickness was used as the separator, and 1 M $NaClO_4$ in propylene carbonate with 5% fluoroethylene carbonate was used as the electrolyte. For the full-cell demonstration, the cathode-active material was NVP-NFs. The one-time discharge/charge cycled 3D graphene served as the anode. The weight ratio between anode and cathode active material was ≈0.72:1. Galvanostatic charge/discharge measurements were carried out on a multichannel battery testing system (LAND CT2001A, China) at different

current densities. Both the charge and discharge current density and specific capacity were calculated based on the mass of cathode-active material. The cyclic voltammetry tests were also conducted on an electrochemical workstation (CHI660E, China). The electrochemical impedance spectroscopy data of the electrodes were acquired at room temperature using a ZAHNER-IM6ex electrochemical workstation (ZAHNER Co., Germany) in the frequency range of 100 kHz to 0.01 Hz on a cell under the as-assembled condition.

## Supporting Information

Supporting Information is available from the Wiley Online Library or from the author.

## Acknowledgements

This work was supported by the National Natural Science Foundation of China (Grant Nos. 51374255, 51302323, and 51572299), the Program for New Century Excellent Talents in University (Grant No. NCET-13-0594), the Research Fund for the Doctoral Program of Higher Education of China (Grant No. 201301621200), the Natural Science Foundation of Hunan Province, China (Grant No. 14JJ3018), and the Fundamental Research Funds for the Central Universities of Central South University (Grant No. 2017zzts109). J.L. would like to acknowledge the support from the Office of Basic Energy Sciences, Division of Materials Sciences and Engineering, U.S. Department of Energy under Award KC020105-FWP12152 for providing technical assistance in the synthesis, characterization, and electrochemical measurement of the materials.

## Conflict of Interest

The authors declare no conflict of interest.

## Keywords

graphene-like cages, nanoflake arrays, $Na_3V_2(PO_4)$, sodium-ion batteries, surfactant

Received: March 23, 2017
Revised: May 7, 2017
Published online: July 14, 2017

[1] V. Palomares, P. Serras, I. Villaluenga, K. B. Hueso, J. Carretero-González, T. Rojo, *Energy Environ. Sci.* **2012**, *5*, 5884.
[2] N. Yabuuchi, K. Kubota, M. Dahbi, S. Komaba, *Chem. Rev.* **2014**, *114*, 11636.
[3] D. Chao, C. Zhu, P. Yang, X. Xia, J. Liu, J. Wang, X. Fan, S. V. Savilov, J. Lin, H. J. Fan, Z. X. Shen, *Nat. Commun.* **2016**, *7*, 12122.
[4] X. Xiang, K. Zhang, J. Chen, *Adv. Mater.* **2015**, *27*, 5343.
[5] H. Pan, Y.-S. Hu, L. Chen, *Energy Environ. Sci.* **2013**, *6*, 2338.
[6] M. Armand, J. M. Tarascon, *Nature* **2008**, *451*, 652.
[7] Z. Yang, J. Zhang, M. C. Kintner-Meyer, X. Lu, D. Choi, J. P. Lemmon, J. Liu, *Chem. Rev.* **2011**, *111*, 3577.
[8] B. Dunn, H. Kamath, J. M. Tarascon, *Science* **2011**, *334*, 928.
[9] D. Kundu, E. Talaie, V. Duffort, L. F. Nazar, *Angew. Chem., Int. Ed.* **2015**, *54*, 3431.
[10] Y. Sun, L. Zhao, H. Pan, X. Lu, L. Gu, Y. S. Hu, H. Li, M. Armand, Y. Ikuhara, L. Chen, X. Huang, *Nat. Commun.* **2013**, *4*, 1870.
[11] N. Yabuuchi, M. Kajiyama, J. Iwatate, H. Nishikawa, S. Hitomi, R. Okuyama, R. Usui, Y. Yamada, S. Komaba, *Nat. Mater.* **2012**, *11*, 512.
[12] Y. Wang, X. Yu, S. Xu, J. Bai, R. Xiao, Y. S. Hu, H. Li, X. Q. Yang, L. Chen, X. Huang, *Nat. Commun.* **2013**, *4*, 2365.
[13] D. Chao, P. Liang, Z. Chen, L. Bai, H. Shen, X. Liu, X. Xia, Y. Zhao, S. V. Savilov, J. Lin, Z. X. Shen, *ACS Nano* **2016**, *10*, 10211.
[14] Y. Zhang, A. Pan, L. Ding, Z. Zhou, Y. Wang, S. Niu, S. Liang, G. Cao, *ACS Appl. Mater. Interfaces* **2017**, *9*, 3624.
[15] Y. Cao, L. Xiao, W. Wang, D. Choi, Z. Nie, J. Yu, L. V. Saraf, Z. Yang, J. Liu, *Adv. Mater.* **2011**, *23*, 3155.
[16] R. Berthelot, D. Carlier, C. Delmas, *Nat. Mater.* **2011**, *10*, 74.
[17] Y. Fang, L. Xiao, J. Qian, X. Ai, H. Yang, Y. Cao, *Nano Lett.* **2014**, *14*, 3539.
[18] X. Rui, W. Sun, C. Wu, Y. Yu, Q. Yan, *Adv. Mater.* **2015**, *27*, 6670.
[19] J. Kim, D. H. Seo, H. Kim, I. Park, J. K. Yoo, S. K. Jung, Y. U. Park, W. A. Goddard Iii, K. Kang, *Energy Environ. Sci.* **2015**, *8*, 540.
[20] P. Senguttuvan, G. Rousse, M. E. Arroyo y de Dompablo, H. Vezin, J. M. Tarascon, M. R. Palacin, *J. Am. Chem. Soc.* **2013**, *135*, 3897.
[21] Y. Fang, L. Xiao, X. Ai, Y. Cao, H. Yang, *Adv. Mater.* **2015**, *27*, 5895.
[22] Y. Fang, L. Xiao, J. Qian, Y. Cao, X. Ai, Y. Huang, H. Yang, *Adv. Energy Mater.* **2016**, *6*, 1502197.
[23] P. Barpanda, G. Oyama, S. Nishimura, S. C. Chung, A. Yamada, *Nat. Commun.* **2014**, *5*, 4358.
[24] P. Singh, K. Shiva, H. Celio, J. B. Goodenough, *Energy Environ. Sci.* **2015**, *8*, 3000.
[25] P. Barpanda, G. Oyama, C. D. Ling, A. Yamada, *Chem. Mater.* **2014**, *26*, 1297.
[26] Y. U. Park, D. H. Seo, H. S. Kwon, B. Kim, J. Kim, H. Kim, I. Kim, H. I. Yoo, K. Kang, *J. Am. Chem. Soc.* **2013**, *135*, 13870.
[27] M. Peng, B. Li, H. Yan, D. Zhang, X. Wang, D. Xia, G. Guo, *Angew. Chem., Int. Ed.* **2015**, *54*, 6452.
[28] Y. U. Park, D. H. Seo, H. Kim, J. Kim, S. Lee, B. Kim, K. Kang, *Adv. Funct. Mater.* **2014**, *24*, 4603.
[29] J. Qian, M. Zhou, Y. Cao, X. Ai, H. Yang, *Adv. Energy Mater.* **2012**, *2*, 410.
[30] C. D. Wessells, S. V. Peddada, R. A. Huggins, Y. Cui, *Nano Lett.* **2011**, *11*, 5421.
[31] L. Wang, Y. Lu, J. Liu, M. Xu, J. Cheng, D. Zhang, J. B. Goodenough, *Angew. Chem., Int. Ed.* **2013**, *52*, 1964.
[32] Z. Jian, W. Han, X. Lu, H. Yang, Y.-S. Hu, J. Zhou, Z. Zhou, J. Li, W. Chen, D. Chen, L. Chen, *Adv. Energy Mater.* **2013**, *3*, 156.
[33] Y. Luo, X. Xu, Y. Zhang, Y. Pi, Y. Zhao, X. Tian, Q. An, Q. Wei, L. Mai, *Adv. Energy Mater.* **2014**, *4*, 1400107.
[34] X. Wang, C. Niu, J. Meng, P. Hu, X. Xu, X. Wei, L. Zhou, K. Zhao, W. Luo, M. Yan, L. Mai, *Adv. Energy Mater.* **2015**, *5*, 1500716.
[35] Y. Zhou, X. Rui, W. Sun, Z. Xu, Y. Zhou, W. J. Ng, Q. Yan, E. Fong, *ACS Nano* **2015**, *9*, 4628.
[36] Q. An, F. Xiong, Q. Wei, J. Sheng, L. He, D. Ma, Y. Yao, L. Mai, *Adv. Energy Mater.* **2015**, *5*, 1401963.
[37] W. Ren, Z. Zheng, C. Xu, C. Niu, Q. Wei, Q. An, K. Zhao, M. Yan, M. Qin, L. Mai, *Nano Energy* **2016**, *25*, 145.
[38] K. Saravanan, C. W. Mason, A. Rudola, K. H. Wong, P. Balaya, *Adv. Energy Mater.* **2013**, *3*, 444.
[39] C. Zhu, K. Song, P. A. van Aken, J. Maier, Y. Yu, *Nano Lett.* **2014**, *14*, 2175.
[40] R. Klee, M. J. Aragon, P. Lavela, R. Alcantara, J. L. Tirado, *ACS Appl. Mater. Interfaces* **2016**, *8*, 23151.
[41] L. Zhang, X. Hu, C. Chen, H. Guo, X. Liu, G. Xu, H. Zhong, S. Cheng, P. Wu, J. Meng, Y. Huang, S. Dou, H. Liu, *Adv. Mater.* **2017**, *29*, 1604708.
[42] J. Wang, X. Sun, *Energy Environ. Sci.* **2015**, *8*, 1110.
[43] C. Wu, P. Kopold, Y. L. Ding, P. A. van Aken, J. Maier, Y. Yu, *ACS Nano* **2015**, *9*, 6610.

 

[44] D. Choi, D. Wang, I. T. Bae, J. Xiao, Z. Nie, W. Wang, V. V. Viswanathan, Y. J. Lee, J. G. Zhang, G. L. Graff, Z. Yang, J. Liu, *Nano Lett.* **2010**, *10*, 2799.
[45] S. Liang, X. Cao, Y. Wang, Y. Hu, A. Pan, G. Cao, *Nano Energy* **2016**, *22*, 48.
[46] M. Chen, W. Ding, Y. Kong, G. Diao, *Langmuir* **2008**, *24*, 3471.
[47] Z. Deng, L. Cao, F. Tang, B. Zou, *J. Phys. Chem. B* **2005**, *109*, 16671.
[48] P. K. Khanna, T. S. Kale, M. Shaikh, N. K. Rao, C. V. V. Satyanarayana, *Mater. Chem. Phys.* **2008**, *110*, 21.
[49] C. Z. Wu, Y. Xie, L. Y. Lei, S. Q. Hu, C. Z. OuYang, *Adv. Mater.* **2006**, *18*, 1727.
[50] M. Yu, Y. Zeng, Y. Han, X. Cheng, W. Zhao, C. Liang, Y. Tong, H. Tang, X. Lu, *Adv. Funct. Mater.* **2015**, *25*, 3534.
[51] Y. Xu, L. Zheng, C. Wu, F. Qi, Y. Xie, *Chem. - Eur. J.* **2011**, *17*, 384.
[52] Y. Zhao, L. Peng, B. Liu, G. Yu, *Nano Lett.* **2014**, *14*, 2849.
[53] J. Yang, H. Wang, P. Hu, J. Qi, L. Guo, L. Wang, *Small* **2015**, *11*, 3744.
[54] J. R. Miller, P. Simon, *Science* **2008**, *321*, 651.
[55] C. Zhong, Y. Deng, W. Hu, J. Qiao, L. Zhang, J. Zhang, *Chem. Soc. Rev.* **2015**, *44*, 7484.
[56] S. W. Oh, S. T. Myung, S. M. Oh, K. H. Oh, K. Amine, B. Scrosati, Y. K. Sun, *Adv. Mater.* **2010**, *22*, 4842.
[57] Z. Li, Z. Peng, H. Zhang, T. Hu, M. Hu, K. Zhu, X. Wang, *Nano Lett.* **2016**, *16*, 795.
[58] Y. J. Lee, H. Yi, W. J. Kim, K. Kang, D. S. Yun, M. S. Strano, G. Ceder, A. M. Belcher, *Science* **2009**, *324*, 1051.
[59] D. Yuan, X. Liang, L. Wu, Y. Cao, X. Ai, J. Feng, H. Yang, *Adv. Mater.* **2014**, *26*, 6301.
[60] Q. Liu, D. Wang, X. Yang, N. Chen, C. Wang, X. Bie, Y. Wei, G. Chen, F. Du, *J. Mater. Chem. A* **2015**, *3*, 21478.
[61] K. Tang, L. Fu, R. J. White, L. Yu, M.-M. Titirici, M. Antonietti, J. Maier, *Adv. Energy Mater.* **2012**, *2*, 873.
[62] H. Hou, C. E. Banks, M. Jing, Y. Zhang, X. Ji, *Adv. Mater.* **2015**, *27*, 7861.
[63] Y. Cao, L. Xiao, M. L. Sushko, W. Wang, B. Schwenzer, J. Xiao, Z. Nie, L. V. Saraf, Z. Yang, J. Liu, *Nano Lett.* **2012**, *12*, 3783.
[64] J. Ding, H. Wang, Z. Li, A. Kohandehghan, K. Cui, Z. Xu, B. Zahiri, X. Tan, E. M. Lotfabad, B. C. Olsen, D. Mitlin, *ACS Nano* **2013**, *7*, 11004.